Atmósfera 40, 75-93 (2026)
https://doi.org/10.20937/ATM.53508

Robust thermodynamic signatures of the Indian ocean high during DJF: A Monte Carlo-based correlation and composite analysis

Nasir ILYAS[1]*, Muhammad JAWED IQBAL[1] and Muhammad FAISAL RIAZ[2]

[1] *Institute of Space Science and Technology (ISST), University of Karachi, Karachi, 75270, Sindh, Pakistan.*
[2] *Department of Computer Science, National University of Computer and Emerging Sciences (FAST-NUCES), Karachi, 75400, Sindh, Pakistan.*
*Corresponding author; email: nasir.ilyaaz@gmail.com

Received: June 15, 2025; Accepted: October 28, 2025

RESUMEN

Este estudio investiga el papel del sistema de alta presión del Océano Índico (IOHP, por su sigla en inglés) en la modulación de los flujos turbulentos de calor en la superficie—específicamente el flujo de calor latente (LHF) y el flujo de calor sensible (SHF)—en el sudeste del Océano Índico durante el verano austral (diciembre-enero-febrero) a lo largo del periodo 1988-2017. El IOHP se caracteriza mediante un marco de centro de acción (COA) para cuantificar su intensidad, extensión latitudinal y magnitud de la presión. Nuestros resultados muestran que el LHF presenta una disminución a largo plazo estadísticamente significativa durante 1988-2017, mientras que el SHF exhibe solo una variabilidad interanual débil sin una tendencia consistente. Este comportamiento contrastante pone de relieve que la refrigeración por evaporación domina los cambios de largo plazo en los flujos, mientras que el SHF permanece secundario. El análisis a largo plazo revela una tendencia descendente significativa del LHF, estrechamente vinculada con reducciones en la presión, y en la cobertura espacial del IOHP. En contraste, el SHF muestra una variabilidad más débil sin una tendencia coherente. Los diagnósticos compuestos basados en fases altas y bajas del IOHP muestran reducciones de LHF y SHF en 15-30º S y 65-95º E durante los años con IOHP intensificado, lo que indica una mayor estabilidad atmosférica y una disminución del flujo de humedad superficial. Estos resultados están respaldados por pruebas de significancia mediante simulaciones de Monte Carlo. Además, los diagramas de dispersión ilustran relaciones inversas fuertes entre la presión del IOHP y el LHF ($r \approx -0.93$), lo que subraya el control del IOHP sobre los procesos de evaporación. Los análisis de correlación sin tendencia con teleconexiones dominantes (incluidas El Niño-Oscilación del Sur, el Dipolo del Océano Índico, el Modo Anular del Sur y el Anticiclón del Pacifico Sur) destacan interacciones específicas por modo, con el IOHP actuando como mediador regional de una variabilidad climática más amplia. Este trabajo demuestra que el debilitamiento y contracción del IOHP podrían agravar el calentamiento superficial y reducir el acoplamiento océano-atmósfera, con posibles implicaciones para el hidroclima regional y el balance energético en Australia occidental.

ABSTRACT

This study investigates the role of the Indian Ocean High Pressure (IOHP) system in modulating surface turbulent heat fluxes—specifically latent heat flux (LHF) and sensible heat flux (SHF)—across the southeastern Indian Ocean during the austral summer (DJF) over the 1988-2017 period. The IOHP is characterized using a center-of-action (COA) framework to quantify its intensity, latitudinal extent, and pressure magnitude. Our findings show that LHF exhibits a statistically significant long-term decline during 1988-2017, whereas SHF demonstrates only weak interannual variability with no consistent trend. This contrasting behavior highlights that evaporative cooling dominates the long-term flux changes, while SHF remains secondary.

Long-term analysis reveals a statistically significant downward trend in LHF, closely linked to reductions in IOHP pressure and spatial coverage. In contrast, SHF exhibits weaker variability with no consistent trend. Composite diagnostics based on high and low IOHP phases show suppressed LHF and SHF across 15-30º S and 65-95º E during intensified IOHP years, indicating enhanced atmospheric stability and reduced surface moisture flux. These results are supported by Monte Carlo significance testing. Further, scatterplots illustrate strong inverse relationships between IOHP pressure and LHF ($r \approx -0.93$), underscoring the IOHP's control on evaporation processes. Detrended correlation analyses with dominant teleconnections—including El Niño-Southern Oscillation, the Indian Ocean Dipole, the Southern Annular Mode, and the South Pacific High—highlight mode-specific interactions, with the IOHP acting as a regional mediator of broader climate variability. This work demonstrates that a weakening and contraction of the IOHP could exacerbate surface warming and reduce ocean-atmosphere coupling, with potential implications for regional hydroclimate and energy balance over western Australia.

Keywords: Indian Ocean High Pressure (IOHP), latent heat flux (LHF), sensible heat flux (SHF), air-sea thermodynamic interaction, Monte Carlo significance testing, center of action (COA) analysis, ocean-atmosphere coupling, climate teleconnections.

1. Introduction

The subtropical anticyclones play a critical role in shaping the surface energy balance and hydrological cycle of the Southern Hemisphere, particularly during the austral summer season (December-February, DJF). Among them, the Indian Ocean High Pressure (IOHP) system—centered over the southwestern Indian Ocean—acts as a major atmospheric center of action, governing moisture transport, wind regimes, and ocean-atmosphere energy exchange (Alexander and Arblaster, 2009; Tandon et al., 2013).

The IOHP is typically defined by sea level pressure exceeding 1020 hPa, and is considered a semi-permanent anticyclone within the subtropical ridge belt. As one of the dominant centers of action (COAs) in the Southern Hemisphere, it exerts strong control on regional circulation, moisture availability, and surface heat fluxes. Variations in the intensity and position of this subtropical high are increasingly recognized as significant contributors to interannual and decadal climate anomalies over Australia, especially regarding surface turbulent heat fluxes such as latent heat flux (LHF) and sensible heat flux (SHF) (Rehman et al., 2019, 2024; van Niel 2024).

LHF and SHF represent key components of the surface energy budget, directly influencing atmospheric temperature, boundary layer stability, and convective potential. Changes in these fluxes are often linked to shifts in large-scale circulation patterns and regional high-pressure systems (Timbal and Drosdowsky, 2013; Holbrook et al., 2019). In the southeastern Indian Ocean, persistent high-pressure anomalies tend to suppress evaporation by stabilizing the lower troposphere and reducing surface wind speeds (Marshall, 2013). This suppression leads to weakened evaporative cooling, potentially intensifying heatwaves and increasing mean surface temperatures over adjacent land regions, including western Australia (Perkins-Kirkpatrick et al., 2016; Power and Delage, 2018).

In addition to local high-pressure dynamics, remote climate drivers such as the El Niño-Southern Oscillation (ENSO), Indian Ocean Dipole (IOD), and Southern Annular Mode (SAM) interact with the IOHP system to produce complex climate outcomes. For instance, El Niño phases often suppress convection over the eastern Indian Ocean, modulating the strength of the subtropical high and its impact on heat fluxes (Stuecker et al., 2013; Lim et al., 2016). Meanwhile, the IOD—although more active in September-November (SON)—can influence the LHF variability during DJF through lingering basin-wide sea surface temperature gradients (Saji et al., 1999; Morioka et al., 2018). SAM, as the dominant annular mode of the Southern Hemisphere, affects the latitudinal displacement of the subtropical ridge and indirectly modifies the IOHP's structure and strength (Arblaster et al., 2011; Yang et al., 2023).

Despite the acknowledged importance of these drivers, few studies have simultaneously examined how the spatiotemporal variability of the IOHP system—in terms of its pressure, latitude, and

longitude—affects surface turbulent fluxes over the southeastern Indian Ocean, particularly during DJF. Existing literature primarily focuses on rainfall and temperature extremes over Australia without systematically quantifying the thermodynamic and dynamic coupling mechanisms linked to the IOHP (Romanski and Hameed, 2015; Pepler and Rudeva, 2023). Moreover, the compound effects of IOHP variations and teleconnection modes on surface flux patterns remain poorly constrained.

This study primarily aims to quantify how the IOHP system shapes surface turbulent fluxes during the austral summer. We focus on how variations in IOHP intensity and position influence evaporation (LHF) and near-surface heat transfer (SHF) across the southeastern Indian Ocean. Framing the analysis in this way highlights the thermodynamic pathways through which subtropical anticyclones regulate regional energy exchange and hydroclimate.

To address this gap, the present study investigates the trends, interannual variability, and dynamic-thermodynamic impacts of the IOHP system on LHF and SHF over the southeastern Indian Ocean during DJF from 1988 to 2017. Using a combination of pressure center diagnostics, correlation analysis, and Monte Carlo-based composite mapping, we evaluate how IOHP phases interact with climate modes such as ENSO, SAM, IOD, and the South Pacific High (SPH), and how these interactions modulate surface energy exchange across oceanic and coastal regions adjacent to Australia.

2. Data and methodology

2.1 Study region and period

The ocean, encompassing the domain 60-120º E and 40-10º S, an area influenced by the IOHP system. The analysis is conducted for the austral summer season—December to February (DJF)—over the 30-year period from 1988 to 2017. This region is characterized by strong subtropical anticyclonic circulations that influence surface heat exchange, making it a relevant domain for investigating the relationship between high-pressure dynamics and surface turbulent fluxes (Pepler et al., 2019).

2.2 Datasets

A suite of reanalysis and observationally constrained datasets was used.

2.2.1 Surface turbulent heat fluxes

LHF and SHF data were obtained from the Objectively Analyzed Air-Sea Fluxes (OAFlux) dataset (Yu and Weller, 2007), provided at 1º × 1º resolution. DJF means were calculated for 1988-2017.

2.2.2 Atmospheric variables

In this study, near-surface specific humidity (Qa), air temperature (Ta), and horizontal wind components (U, V) at 1000 hPa were taken from the NCEP/NCAR Reanalysis 1 dataset (Kalnay et al., 1996). This dataset was selected because it covers a long period beginning in 1948, making it useful for studying changes and variability over many decades. Although ERA5 (Hersbach et al., 2020) offers better detail in space and time, it only begins in 1979. Since our aim was to look at long-term variability and trends in surface heat fluxes, the longer NCEP/NCAR record was more appropriate for this research.

2.2.3 Sea level pressure (SLP)

SLP data were also sourced from NCEP/NCAR and used to compute IOHP indices using the center of action (COA) method following Romanski and Hameed (2015).

2.2.4 Climate teleconnection indices

DJF-averaged values for Niño 3.4, the SAM (Marshall, 2003), and IOD (Saji et al., 1999) were included to evaluate broader influences. All indices were linearly detrended (Murphy and Timbal 2008; Power and Delage 2018).

2.3 Indian Ocean high pressure (IOHP) indices

The IOHP system was described using the COA framework across the region 60-120º E and 40-10º S. The indices mentioned below were calculated following the departure of seasonal SLP from a set threshold (P_t = 1020 hPa) according to the methodology suggested by Romanski and Hameed (2015).

To describe the IOHP system, we developed three distinct indices. While the latitude (IOH_LAT) and longitude (IOH_LON) indices quantify the system's core shifts from east to west and north to south, the pressure index (IOH_P) measures the system's average strength. Taken together, these measurements provide a precise numerical representation of the IOHP's intensity and geographic variation over time.

$$\text{Pressure Index} : IOH\_P = \frac{\sum_{i.j=1}^{IJ}(P_{ij}-P_t).cos\varnothing_{ij}.\delta_{ij}}{\sum_{i.j=1}^{IJ}cos\varnothing_{ij}.\delta_{ij}} \quad (1)$$

$$\text{Latitude Index} : IOH\_LAT = \frac{\sum_{i,j=1}^{IJ}(P_{ij}-P_t).\varnothing_{ij}.\cos\varnothing_{ij}.\delta_{ij}}{\sum_{i,j=1}^{IJ}\left(P_{ij}-P_t\right).\cos\varnothing_{ij}.\delta_{ij}} \quad (2)$$

$$\text{Longitude Index} : IOH\_LON = \frac{\sum_{i,j=1}^{IJ}(P_{ij}-P_t).l_{ij}.\cos\varnothing_{ij}.\delta_{ij}}{\sum_{i,j=1}^{IJ}(P_{ij}-P_t).\cos\varnothing_{ij}.\delta_{ij}} \quad (3)$$

In this case, if $(P_{ij} - P_t) > 0$, $\delta_{ij} = 1$; otherwise, $\delta_{ij} = 0$. The intensity of IOHP is represented by *IOH_P*, while its horizontal displacement during the study period is represented by *IOH_LAT*, and *IOH_LON*.

The COA approach is superior to fixed pressure readings for assessing the movement and strength of subtropical highs. It facilitates tracking the center of the IOHP across seasons and demonstrates how its variations are connected to variations in heat flow. This approach has also been employed in previous research on subtropical highs (Romanski and Hameed, 2015; Alam et al., 2021). This approach to examining the IOHP system is now widely accepted. It monitors latitude and longitude variations, providing a clear picture of seasonal changes and enabling a more objective analysis of IOHP behavior.

2.4 Composite analysis

To evaluate the physical mechanisms associated with high- and low-IOHP phases, composite differences were computed for the following key variables: (*i*) Moisture gradient (Qa – Qs [g kg^{-1}]), (*ii*) Temperature gradient (Ta – Ts [ºC]), (*iii*) zonal and meridional winds (U, V), and (*iv*) surface turbulent fluxes (LHF, SHF [W m^{-2}]).

High and low years were defined based on the median split of the IOHP indices. Differences were calculated as:

$$\Delta = \text{Mean}_{\text{high}} - \text{Mean}_{\text{low}} \quad (4)$$

Statistical significance was assessed using Monte Carlo simulations (1000 permutations), and only differences passing a 95% confidence threshold ($p \leq 0.05$) were retained. This approach ensures robust detection of thermodynamic and dynamic anomalies (Wilks, 2016).

2.5 Correlation analysis

Pearson correlations were computed between detrended heat flux time series and IOHP indices. Following common practice in climate diagnostics (Wilks, 2016), a threshold of $|r| \geq 0.3$ was applied as a heuristic guide to indicate potentially meaningful relationships, while formal statistical significance was assessed separately using Pearson correlation tests with effective degrees of freedom. Spatial correlation fields were also constructed between LHF/SHF and key teleconnection indices (SAM, IOD, Niño 3.4), placing IOHP variability in the broader context of large-scale atmospheric circulation. All analyses were performed using Matlab (MathWorks, 2023).

This integrated methodology enables a comprehensive evaluation of how IOHP variability modulates surface turbulent fluxes in the southeastern Indian Ocean, using physically grounded and statistically validated diagnostics.

3. Results

3.1 Climatological structure of the Indian Ocean High Pressure

The climatological mean sea level pressure (SLP) during the austral summer (DJF) for the period 1988-2017 shows the presence of a well-defined subtropical high centered over the southeastern Indian Ocean (Fig. 1). The high-pressure core is located near 80 and 33º S, with a central pressure exceeding 1020 hPa. The closed isobaric structure defines the IOHP system, which exerts a dominant influence on regional heat flux variability and wind patterns. This spatial pattern justifies the domain selection (60-120º E, 40-10º S) used in subsequent analyses.

3.2 Interannual variability of IOHP indices

Figure 2 presents the interannual variability of the IOHP pressure, latitude, and longitude indices for the DJF season during 1988-2017. The pressure index (Fig. 2a) shows a weak decreasing trend over the period, although with considerable interannual fluctuations. This behavior is broadly consistent with (Simmonds and Li, 2021), who reported DJF interannual variability of ~1.5 hPa in the IOH region and daily fluctuations of 4-6 hPa. Their analysis also showed that summer pressures decreased north of the IOH domain and increased southward, supporting the weak

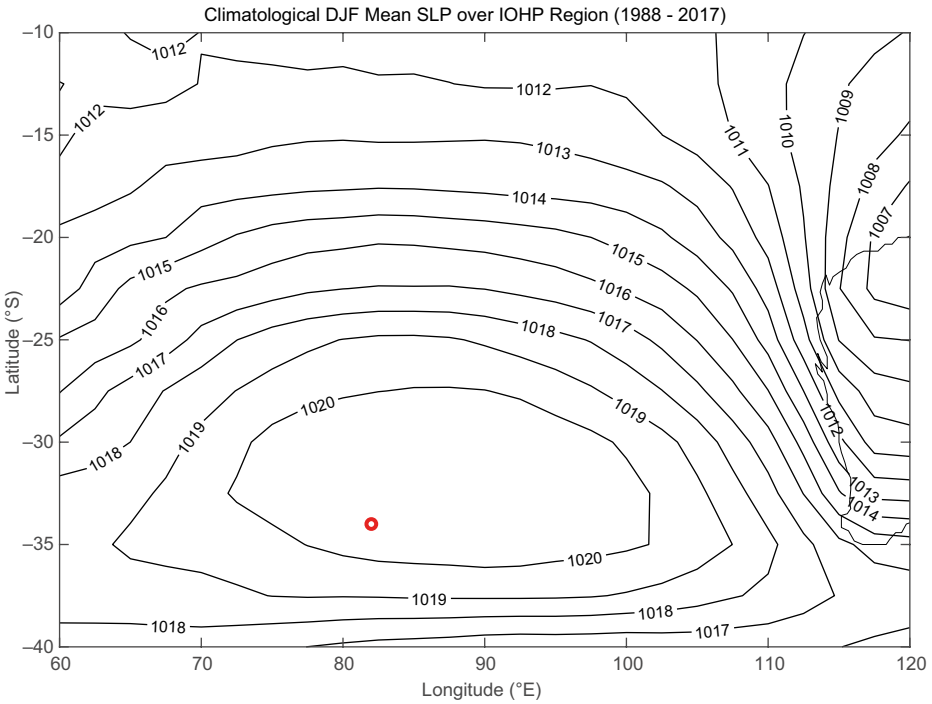

Fig. 1. DJF climatological mean SLP over the IOHP region (60-120º E, 40-10º S) for 1988-2017. Contour intervals are drawn at 1 hPa. The red circle marks the maximum pressure center (1020.9 hPa at 35.0º S, 82.5º E), identifying the IOHP core. (DJF: December, January, February; SLP: sea level pressure; IOHP: Indian Ocean High Pressure.)

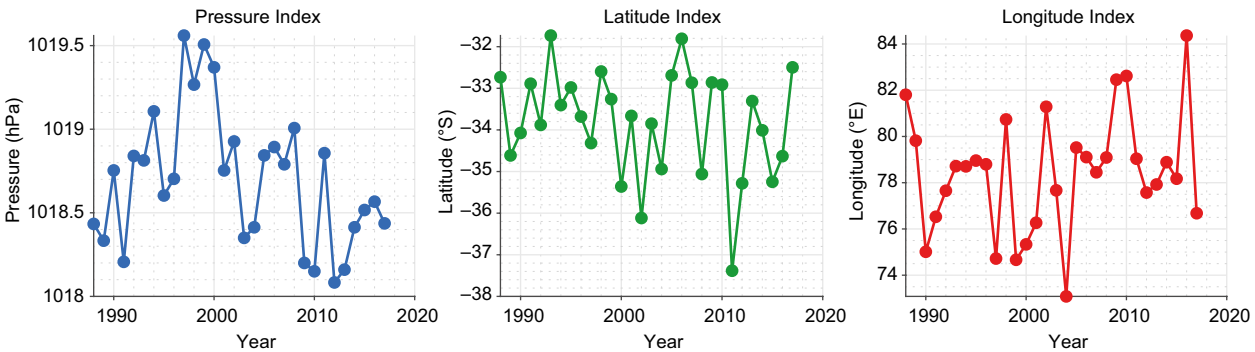

Fig. 2. Time series of DJF IOHP indices from 1988-2017: (a) pressure index (hPa), (b) latitude of IOHP center (ºS), and (c) longitude of IOHP center (ºE). The indices are calculated using the center of action approach over the domain 60-120º E and 40-10º S. (DJF: December, January, February; IOHP: Indian Ocean High Pressure).

poleward displacement observed here. Furthermore, Rudeva et al. (2019) demonstrated that such modest poleward shifts in subtropical highs are dynamically linked with the poleward migration of the Southern Hemisphere synoptic activity, reinforcing our interpretation of IOHP variability. The latitude index (Fig. 2b) exhibits a weak southward shift, reflecting minor meridional displacement of the IOHP center. Similarly, the longitude index (Fig. 2c) indicates intermittent eastward shifts, suggesting spatial variability in the zonal positioning of the high-pressure core. These shifts may influence regional surface fluxes through changes in wind direction and magnitude, as further discussed in subsequent sections.

3.3 Relationship between IOHP pressure and position

To explore the spatial variability of the IOHP system, scatterplots between the SLP index and its corresponding latitude and longitude positions are shown in Figure 3. The SLP vs. latitude relationship (Fig. 3a) displays a weak negative association, while the SLP vs. longitude relationship (Fig. 3b) reveals a slightly stronger negative spread, suggesting that lower pressure years are generally associated with eastward shifts of the high-pressure core. These preliminary relationships are quantified and interpreted in detail in the discussion section.

3.4 Trends in surface turbulent heat fluxes

Figure 4 presents the DJF time series of surface turbulent heat fluxes over the IOHP region from 1988 to

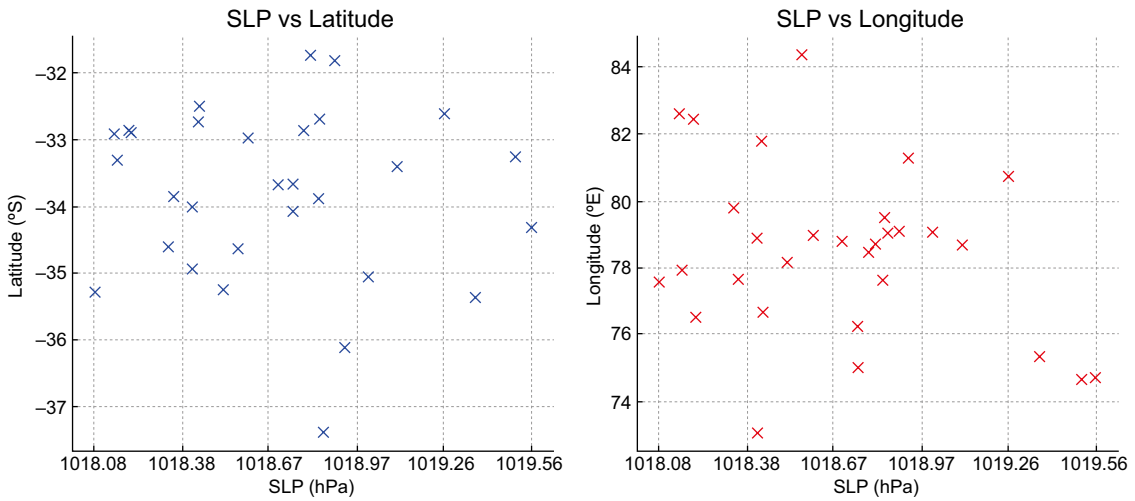

Fig. 3. Scatterplots between IOHP pressure index (SLP) and the center-of-action (a) latitude and (b) longitude during DJF (1988-2017). Each point represents one DJF season. Linear correlation coefficients are discussed in Section. (IOHP: Indian Ocean High Pressure; SLP: sea level pressure; DJF: December, January, February.)

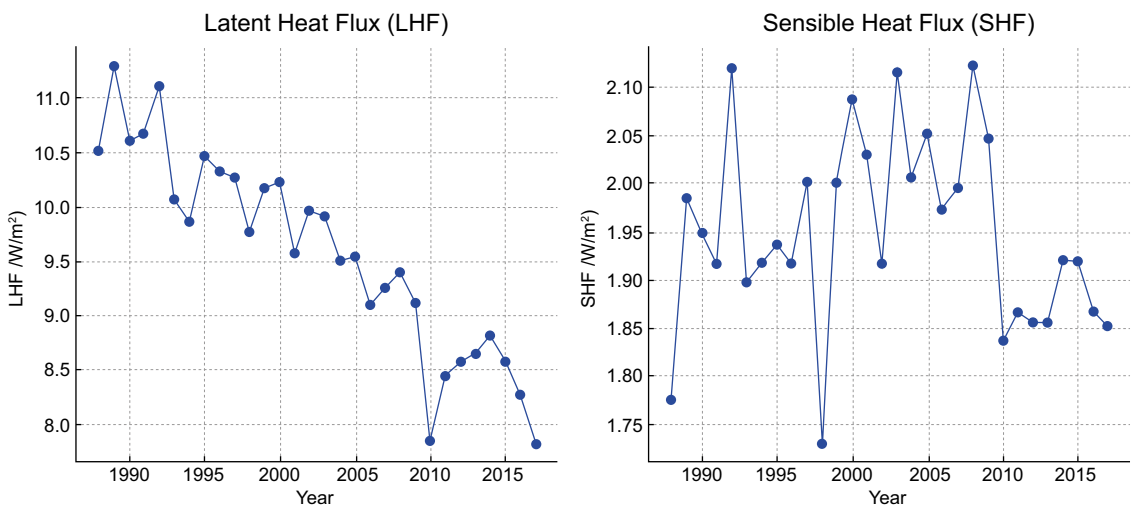

Fig. 4. Time series of DJF (a) LHF and (b) SHF over the IOHP region (60-120º E, 40-10º S) from 1988 to 2017. LHF shows a strong declining trend, while SHF remains largely variable without a consistent trend. (DJF: December, January, February; LHF: latent heat flux; SHF: sensible heat flux; IOHP: Indian Ocean High Pressure.)

2017. The LHF (Fig. 4a) displays a strong decreasing trend, with values declining from above 11 W m^{-2} in the late 1980s to below 8.5 W m^{-2} after 2010. This consistent downward trend suggests a long-term reduction in evaporative cooling, possibly linked to changes in moisture availability and large-scale circulation. In contrast, the SHF (Fig. 4b) exhibits no clear trend, showing substantial interannual variability with no significant long-term increase or decrease. The contrasting behavior of LHF and SHF highlights the dominant role of latent heat exchange in the regional energy balance.

3.5 Interannual variability in climate drivers

The SAM, the IOD, and the SPH index exhibit substantial interannual variability, consistent with their known episodic nature. Niño 3.4 and Niño 4 (Fig. 5a-b) show alternating El Niño and La Niña events with no discernible long-term trend. The SAM index (Fig. 5c) remains mostly positive after the mid-1990s, while the IOD index (Fig. 5d) is relatively weak during DJF, with most values near or below 0.2. The SPH index (Fig. 5e) shows variability without a systematic trend, ranging from 1017.5 to over 1020 hPa. These drivers are later examined in relation to heat flux variability across the IOHP region.

3.6 Spatial extent of the IOHP

To evaluate seasonal changes in the area occupied by the IOHP, a normalized spatial extent index was calculated based on the fractional area where SLP exceeded 1020 hPa. As shown in Fig. 6, the spatial coverage of the high peaked around the early 2000s and declined markedly in the 2010s. Values close to 1.0 indicate years

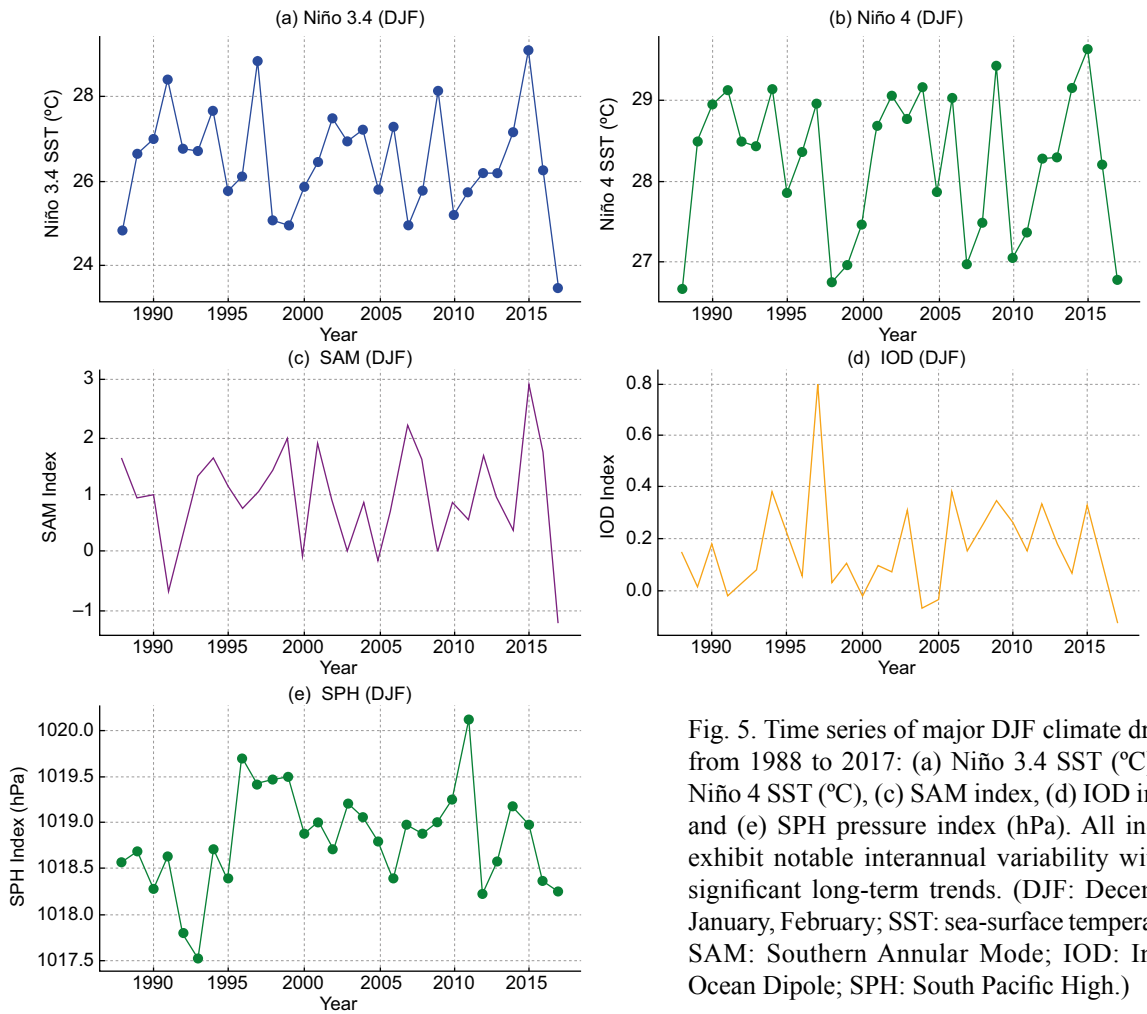

Fig. 5. Time series of major DJF climate drivers from 1988 to 2017: (a) Niño 3.4 SST (ºC), (b) Niño 4 SST (ºC), (c) SAM index, (d) IOD index, and (e) SPH pressure index (hPa). All indices exhibit notable interannual variability without significant long-term trends. (DJF: December, January, February; SST: sea-surface temperature; SAM: Southern Annular Mode; IOD: Indian Ocean Dipole; SPH: South Pacific High.)

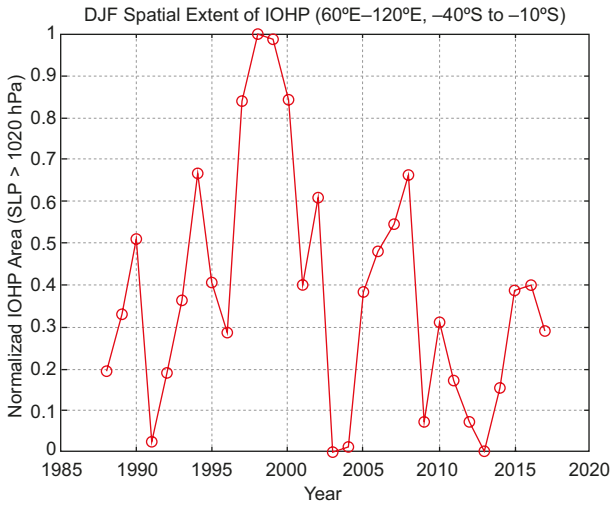

Fig. 6. Normalized DJF spatial extent of the IOHP system over 60-120º E and 40-10º S from 1988 to 2017. The index is defined as the fractional area where SLP exceeds 1020 hPa, normalized by the maximum extent observed during the study period. Values close to 1.0 therefore represent years when the IOvHP reached its broadest coverage relative to the 1988-2017 climatology, rather than indicating that the entire domain exceeded 1020 hPa. Lower values reflect a contracted IOHP spatial footprint. (DJF: December, January, February; IOHP: Indian Ocean High Pressure; SLP: sea level pressure.)

when the IOHP reached its broadest spatial extent relative to the 1988-2017 climatology, rather than implying that the entire domain exceeded the 1020 hPa threshold. Conversely, the post-2010 period shows repeated years with near-zero normalized coverage, indicating a substantial contraction of the IOHP system. These changes may have contributed to the weakening of surface latent heat fluxes observed over the same period.

3.7 Spatial correlation of surface heat fluxes with time

Figure 7 illustrates the spatial correlation between DJF surface turbulent heat fluxes and time across the IOHP domain (60-120º E, 40-10º S), assessed using a Monte Carlo simulation with 1000 permutations. Figure 7a shows a widespread negative correlation (red shading) between LHF and time, particularly concentrated between 65-90º E and 25-35º S. Many of these correlations are statistically significant at the 95% confidence level, as indicated by the black dots.

In contrast, SHF correlations (Fig. 7b) are generally weak and spatially scattered, with no consistent large-scale trend. These results emphasize that the long-term decline in surface turbulent energy exchange over the IOHP region is primarily driven by reductions in latent heat flux, likely linked to changes in air-sea humidity gradient or wind speed.

3.8 Correlation of IOHP characteristics with surface turbulent heat fluxes

To investigate the influence of IOHP variations on surface turbulent heat fluxes, scatterplots were constructed between IOHP indices and LHF and SHF during DJF (1988-2017). Figure 8 illustrates these relationships in terms of pressure, latitude, and longitude indices of the IOHP system. A positive correlation was observed between LHF and IOHP pressure over the southern Indian Ocean, while negative correlations dominated the northern region (Fig. 8a), indicating that a weakening high-pressure system in the north corresponds to enhanced latent heat flux. Similarly, SHF also displayed a north-south dipole in relation to IOHP pressure, with negative correlations to the north and positive to the south (Fig. 8b).

LHF showed a strong negative relationship with IOHP latitude (Fig. 8c), suggesting that an equatorward displacement of the high tends to enhance evaporation, whereas poleward shifts suppress it. SHF latitude correlations were weaker but generally negative across the southern domain (Fig. 8d).

Both fluxes exhibited consistent responses to IOHP longitude: LHF (Fig. 8e) and SHF (Fig. 8f) showed widespread negative correlations, indicating that westward displacement of the high enhances turbulent fluxes, while eastward shifts suppress them.

These results highlight the thermodynamic sensitivity of the Australian region to shifts and intensity changes in the Indian Ocean subtropical high during austral summer.

3.9 Impact of IOD and SAM on surface heat fluxes

To assess the influence of large-scale climate drivers on surface energy exchange, the relationship between detrended latent and sensible heat fluxes and two dominant modes—IOD and SAM—was evaluated

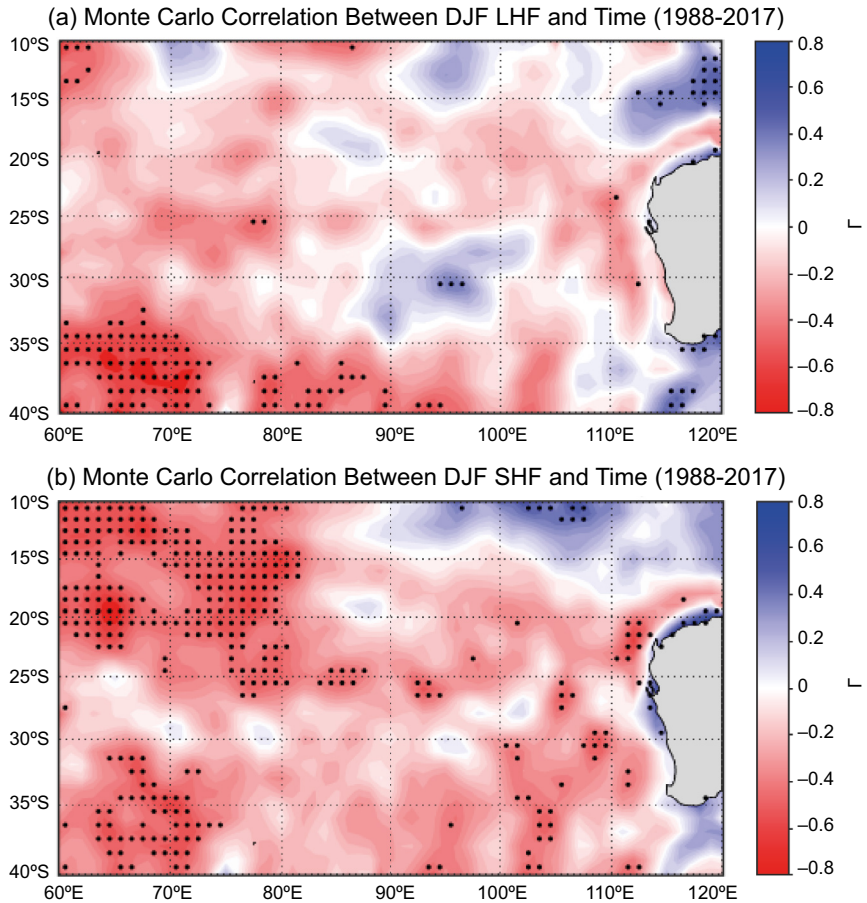

Fig. 7. Monte Carlo correlation between DJF surface turbulent heat fluxes and time over the region 60-120º E, 40-10º S during 1988-2017. (a) Spatial correlation between LHF and time; (b) correlation between SHF and time. Statistical significance is assessed using a Monte Carlo simulation with 1000 random permutations. Black dots indicate grid points where correlations are significant at the 95% confidence level ($p \leq 0.05$). (DJF: December, January, February; LHF: latent heat flux; SHF: sensible heat flux.)

during DJF (1988-2017). The spatial correlation maps are shown in Figure 9 for the domain 60-120º E and 40-10º S.

In Figure 9a, LHF exhibits significant negative correlations with the IOD, particularly over the southeastern Indian Ocean and coastal western Australia. These patterns suggest enhanced latent heat release during negative IOD phases, likely due to increased surface moisture and convective activity. In Figure 9b, SHF correlations with the IOD are weaker but show similar negative tendencies, implying reduced surface warming under enhanced cloud cover or moist conditions.

For SAM, Figure 9c shows that LHF generally correlates negatively in mid-latitude regions, indicating suppressed evaporation during positive SAM events, which are typically associated with poleward shifts of the subtropical ridge. In contrast, Figure 9d reveals modest positive correlations between SHF and SAM, particularly in the western and southern parts of the domain, reflecting warm continental advection linked to the intensified westerlies during high SAM phases.

Overall, Figure 9 highlights the spatially variable and mode-specific sensitivity of surface heat fluxes to hemispheric- and ocean-basin-scale climate drivers during the austral summer.

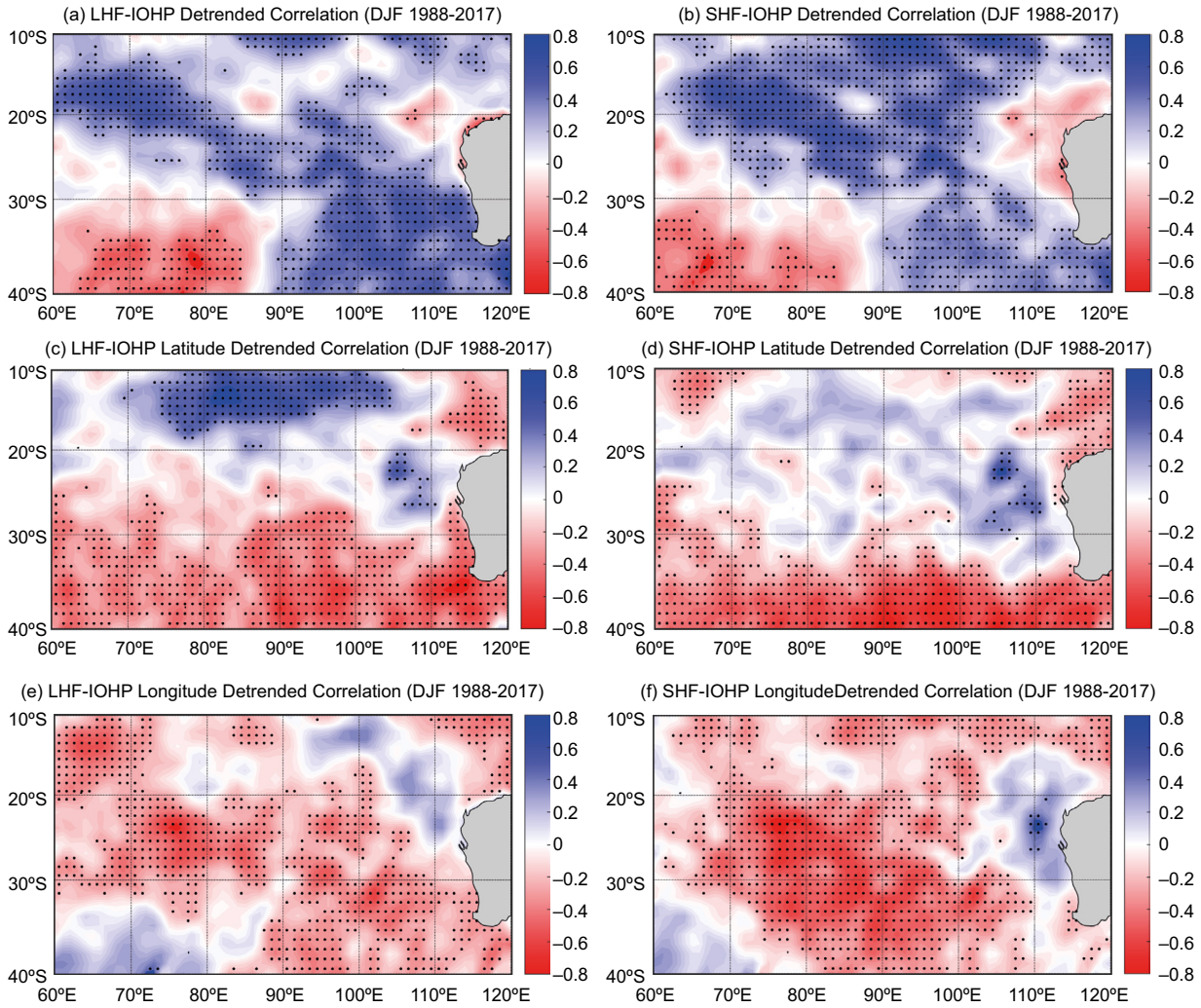

Fig. 8. Correlation maps showing the relationship between surface turbulent heat fluxes and IOHP characteristics during DJF (1988-2017). (a) LHF vs IOHP pressure, (b) LHF vs IOHP latitude, (c) LHF vs IOHP longitude, (d) SHF vs IOHP pressure, (e) SHF vs IOHP latitude, and (f) SHF vs IOHP longitude. Negative correlations in LHF panels suggest enhanced evaporative heat loss under weaker or displaced IOHP systems, indicating a significant thermodynamic response of surface fluxes to pressure anomalies. (IOHP: Indian Ocean High Pressure; LHF: latent heat flux; SHF: sensible heat flux.)

3.10 Influence of ENSO on surface heat fluxes

To evaluate the impact of ENSO on surface turbulent heat fluxes over the southeastern Indian Ocean, correlations were computed between detrended LHF, SHF, and the Niño 3.4 index for the DJF season (1988-2017). These relationships are illustrated in Figure 10.

Figure 10a shows that LHF is significantly negatively correlated with Niño 3.4 across the southern and western parts of the domain, suggesting intensified latent heat release during La Niña episodes. In contrast, regions near the equator and the northwestern Indian Ocean exhibit weak positive correlations.

In Figure 10b, SHF correlations with Niño 3.4 are generally negative over southern latitudes and coastal Australia, reflecting cooler surface conditions during La Niña. Some positive values appear in the tropics but lack spatial coherence.

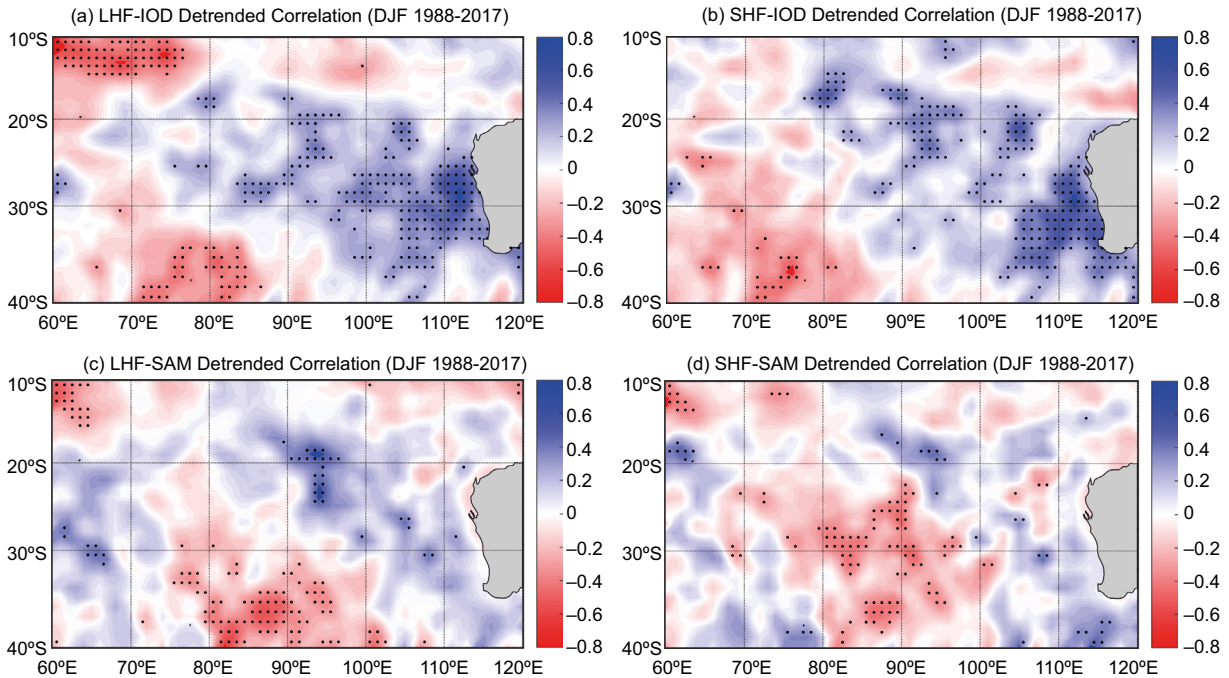

Fig. 9. Spatial correlation between detrended surface turbulent heat fluxes and two major climate indices during DJF (1988-2017): (a) LHF vs IOD, (b) SHF vs IOD, (c) LHF vs SAM, and (d) SHF vs SAM. Correlation coefficients are based on the traditional Pearson method after removing linear trends. Regions with relatively strong positive (red) and negative (blue) associations highlight the impact of IOD and SAM variability on surface heat flux patterns over the southeastern Indian Ocean and coastal Australia. (DJF: December, January, February; LHF: latent heat flux; IOD: Indian Ocean Dipole; SHF: sensible heat flux; SAM: Southern Annular Mode.)

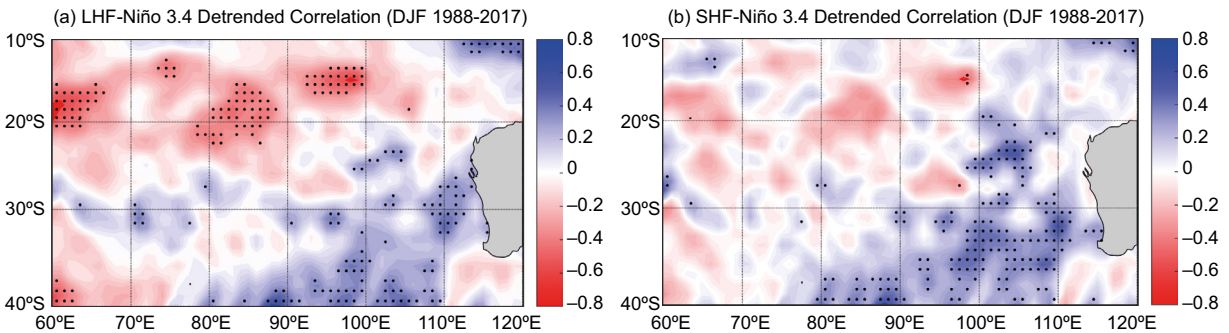

Fig. 10. Spatial correlation between detrended surface turbulent heat fluxes and the Niño 3.4 index during DJF (1988-2017): (a) LHF vs Niño 3.4 and (b) SHF vs Niño 3.4. Correlation coefficients are based on Pearson's method after trend removal. Black dots indicate statistically significant correlations ($p \leq 0.05$). (DJF: December, January, February); LHF: latent heat flux; SHF. sensible heat flux.)

Overall, Figure 10 indicates that ENSO strongly modulates surface fluxes, with La Niña phases promoting stronger evaporation (enhanced LHF) and lower SHF, particularly in southern regions.

3.11 Influence of the South Pacific High on surface heat fluxes

The spatial correlation between the SPH and surface turbulent heat fluxes during DJF (1988-2017)

is shown in Figure 11. In Figure 11a, LHF exhibits negative correlations with SPH over much of the southeastern Indian Ocean, with statistically significant values extending eastward toward the Australian coast.

Similarly, Figure 11b shows that SHF is also negatively correlated with SPH across central and eastern parts of the domain, with notable significant patches aligned with the coastal margins and southern regions.

3.12 Monte Carlo composite differences of thermodynamic and wind fields

Composite differences between high and low phases of the IOHP during DJF (1988-2017) were computed using a Monte Carlo approach to assess statistically robust changes in thermodynamic gradients and near-surface wind structure. The results are presented in Figure 12.

In Figure 12a, the specific humidity gradient (Qa – Qs) exhibits widespread positive anomalies (blue), suggesting enhanced vertical moisture gradients and greater moisture availability under IOHP high conditions.

Figure 12b shows predominantly negative anomalies (red) in the air-sea temperature gradient (Ta – Ts), especially across the central and eastern regions. This indicates colder near-surface air over relatively warmer ocean surfaces during high IOHP years.

For dynamic fields, Figure 12c illustrates negative anomalies (red) in the zonal wind (U), particularly in southern latitudes, reflecting stronger easterly wind anomalies.

In Figure 12d, the meridional wind component (V) shows positive anomalies (blue) centered around 30-40º S and 70-90º E, highlighting anomalous northward flow under high IOHP phases.

3.13 Monte Carlo composite differences of thermodynamic and wind fields

The analysis of Monte Carlo composite difference was conducted between high and low phases of the IOHP during DJF (1988-2017) to assess statistically robust changes in near-surface thermodynamic conditions and wind flow patterns. The results are shown in Figure 13.

In Figure 13a, the composite of specific humidity (Qa) reveals significant negative anomalies across the southeastern Indian Ocean, particularly between 15-35º S, indicating a robust decrease in near-surface humidity during IOHP high years. Anomalous wind vectors indicate a southward and south-eastward flow associated with this dry anomaly.

Figure 13b shows statistically significant positive differences in near-surface air temperature (Ta) across most of the domain, suggesting widespread warming of the lower atmosphere during high IOHP years. Wind vectors depict north-westward anomalies, potentially enhancing warm advection.

These results are based on a Monte Carlo simulation with 1000 random permutations, though significance points are not explicitly marked on this map.

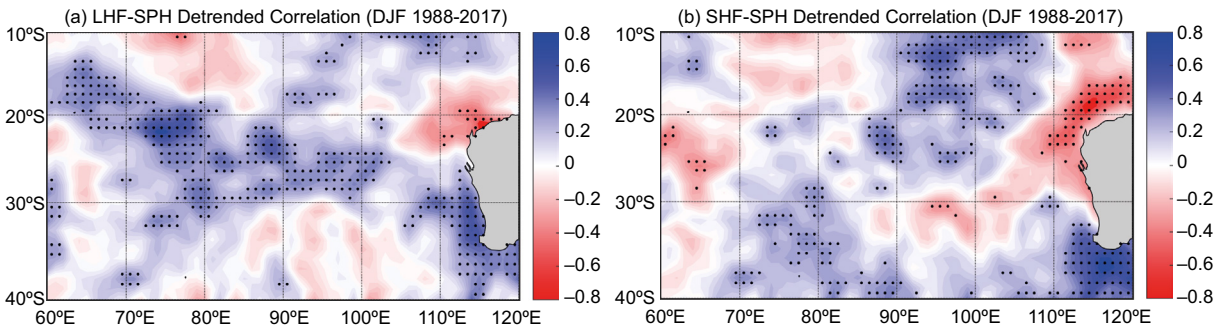

Fig. 11. Detrended spatial correlation between SPH pressure and surface turbulent heat fluxes during DJF (1988-2017): (a) LHF vs SPH and (b) SHF vs SPH. Black dots indicate statistically significant correlations at the 95% level ($p \leq 0.05$). (SPH: South Pacific High; DJF: December, January, February; LHF: latent heat flux; SHF: sensible heat flux.)

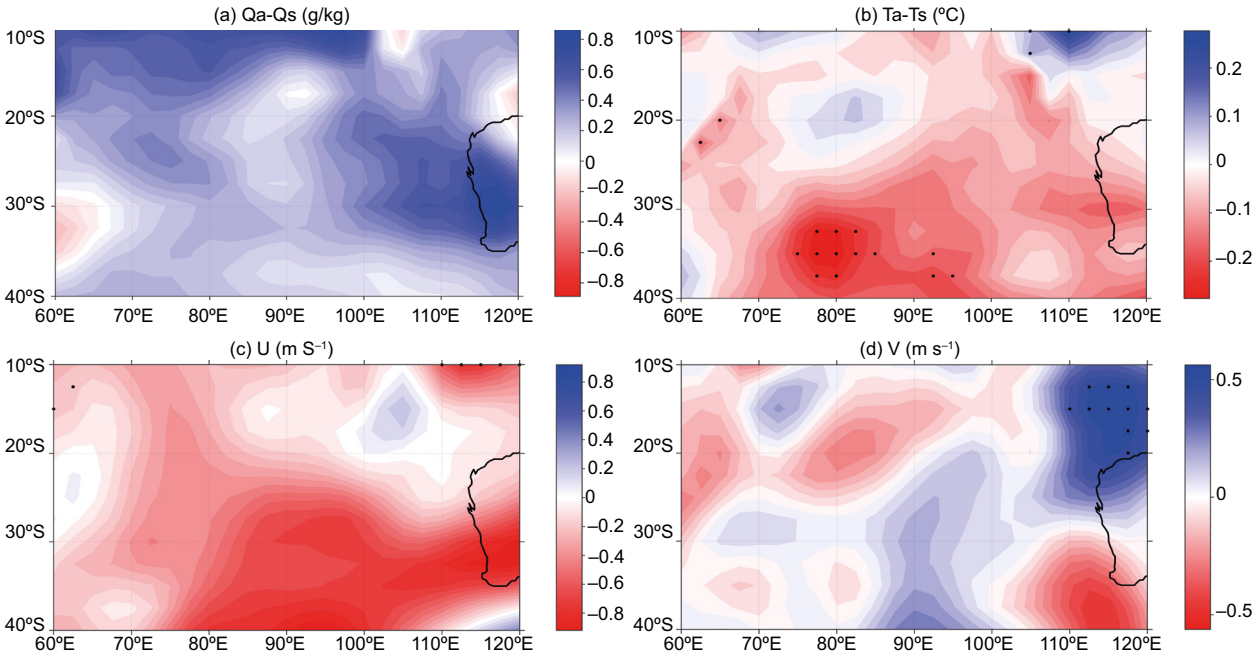

Fig. 12. Monte Carlo composite differences between IOHP high and low phases during DJF (1988-2017): (a) Qa – Qs (g kg^{-1}), (b) Ta – Ts (ºC), (c) zonal wind U (m s^{-1}), (d) meridional wind V (m s^{-1}). Positive values (blue) represent stronger magnitudes during IOHP high years. Black dots indicate regions statistically significant at the 95% confidence level based on 1000 Monte Carlo permutations. (IOHP: Indian Ocean High Pressure; DJF: December, January, February; Qa: near-surface specific humidity; Qs: surface specific humidity; Ta: near-surface air temperature; Ts: surface air temperature.)

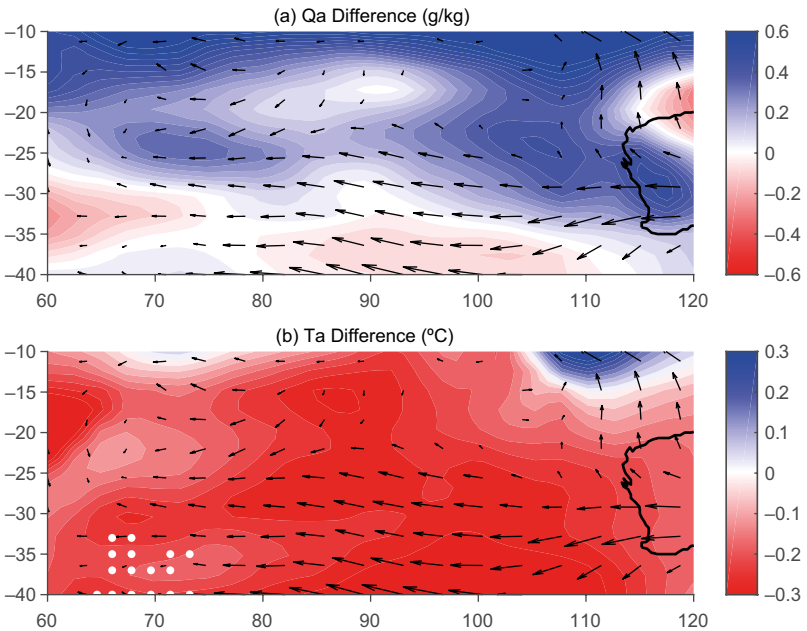

Fig. 13. Monte Carlo composite differences between IOHP high and low phases during DJF (1988-2017): (a) specific humidity difference (Qa, g kg^{-1}) with wind vector anomalies, (b) air temperature difference (Ta, ºC) with wind vector anomalies. Positive values represent higher magnitudes during IOHP high years. Wind arrows (U, V) represent composite vector anomalies. White dots indicate regions where composite differences are statistically significant at the 95% confidence level based on 1000 Monte Carlo permutations. (IOHP: Indian Ocean High Pressure; DJF: December, January, February.)

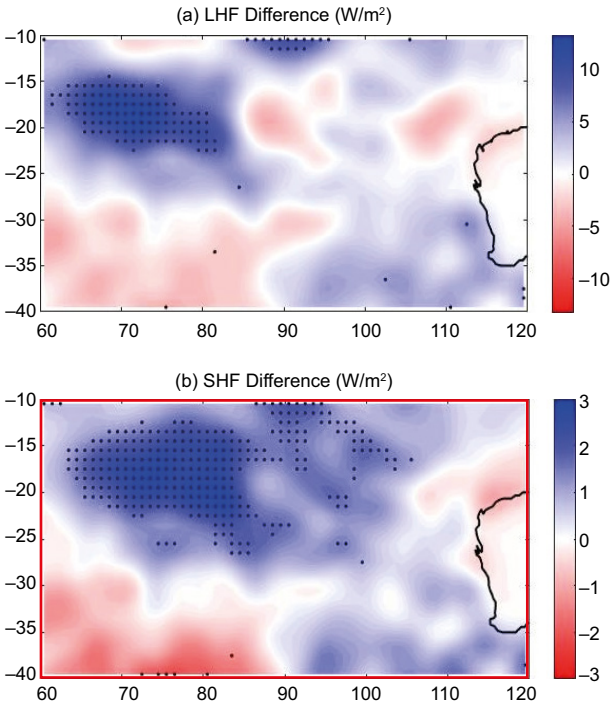

Fig. 14. Monte Carlo composite differences in surface turbulent heat fluxes between IOHP high and low phases during DJF (1988-2017): (a) LHF difference (W m^{-2}), (b) SHF difference (W m^{-2}). Negative values indicate weaker fluxes during IOHP high years. Black dots denote grid points statistically significant at the 95% confidence level. (IOHP: Indian Ocean High Pressure; DJF: December, January, February; LHF: latent heat flux; SHF: sensible heat flux.)

3.14 Monte Carlo composite differences in surface turbulent heat fluxes

Monte Carlo composite differences between high and low years of the IOHP reveal distinct spatial changes in latent and sensible heat fluxes across the southeastern Indian Ocean during DJF (1988-2017).

Figure 14a shows that LHF exhibits significantly negative anomalies across most of the region, especially between 15-30º S and 65-95º E. This pattern indicates suppressed evaporative fluxes during high phases of the IOHP, potentially due to enhanced subsidence and atmospheric stability.

In Figure 14b, SHF also shows negative anomalies, most notably in the tropical latitudes north of 20º S. These reductions suggest reduced vertical heat exchange between ocean and atmosphere under strengthened high-pressure conditions.

Both panels in Figure 14 incorporate Monte Carlo significance testing using 1000 random permutations.

4. Discussion

4.1 IOHP variability and regional heat flux impacts

The IOHP system exhibited notable interannual variability in core intensity and spatial extent during DJF (1988-2017), significantly influencing surface turbulent heat fluxes across the southeastern Indian Ocean (Figs. 2-3). Variability in the IOHP pressure index and core location (latitude and longitude) revealed westward and equatorward shifts, with potential implications for enhanced convergence and latent heat release near the continental boundary. The significant negative correlation between LHF and IOHP central pressure (Fig. 8a) confirms the suppressive role of a strong IOHP on evaporation. This relationship is consistent with the findings of Romanski and Hameed (2015), who highlighted the role of subtropical anticyclones in modulating regional climate patterns through their dynamical positioning. Similar modulations in the Hadley circulation by subtropical ridges were also highlighted by Wills et al. (2018) and Mahlobo et al. (2024).

4.2 Temporal trends in surface fluxes

Time series analysis (Fig. 4) shows a significant declining trend in LHF, indicating decreasing oceanic evaporative cooling across the region, whereas SHF remains largely stationary. These patterns are consistent with the Monte Carlo correlation maps (Fig. 7), reinforcing the long-term reduction in LHF,

particularly under intensified anticyclonic conditions. These results align with the findings of Pepler et al. (2019), who reported similar drying trends associated with persistent subtropical highs, contributing to reduced surface evaporation and greater atmospheric stability. Long-term surface flux trends have also been detected by Sun and Wu (2022) in the global oceans, with spatial heterogeneity driven by changing atmospheric circulation patterns.

4.3 Influence of IOHP dynamics on surface fluxes

Scatterplot analyses (Fig. 8a-c) demonstrate that weaker or displaced IOHP phases correspond with enhanced LHF, confirming the IOHP's regulation of energy exchange across the southeastern Indian Ocean. The declining spatial extent of the IOHP (Fig. 6) likely contributes to reduced LHF through diminished subsidence and weaker divergence over the region. The weak SHF correlations highlight that sensible heat exchange is less directly influenced by IOHP core variability and is more spatially fragmented. These findings align with those of Chiu et al. (2013), who highlighted that SHF is primarily driven by local-scale air-sea temperature differences rather than large-scale circulation patterns. Their satellite-based assessment of surface fluxes demonstrated that while LHF reflects broader atmospheric modulation, SHF remains tightly linked to regional thermodynamic contrasts near the ocean surface.

4.4 Teleconnection modulation of heat fluxes

Correlation analyses (Figs. 9-11) reveal the modulation of LHF and SHF by large-scale climate modes. During negative IOD phases, LHF increases over southeastern and coastal western Australia (Fig. 9a), consistent with increased convection and moisture availability (Saji et al., 1999). Similar results were shown by Ummenhofer et al. (2009), who linked negative IODs to wetter conditions and elevated surface fluxes over western and southern Australia. SAM is associated with negative LHF correlations over mid-latitudes (Fig. 9c) and positive SHF correlations in western sectors (Fig. 9d), supporting interpretations of poleward subtropical ridge shifts and stronger westerlies (Marshall 2003; Hendon et al., 2007).

ENSO's role, shown in Fig. 10, is evident in negative LHF correlations under La Niña phases (Fig. 10a, c), attributed to strengthened Walker circulation and westward convection. SHF shows reduced values across southern latitudes (Fig. 10b, d), further affirming La Niña's cooling effect over the eastern Indian Ocean (Power et al., 2018). These mechanisms were also highlighted by Taschetto and England (2009), who described regional ocean-atmosphere coupling during ENSO events.

4.5 Composite differences in thermodynamic and wind fields

Monte Carlo-based composite diagnostics (Fig. 12) between IOHP high and low years reveal thermodynamic gradients indicative of enhanced atmospheric stability. Positive Qa-Qs anomalies (Fig. 12a; blue shading) suggest strong vertical moisture stratification, while negative Ta-Ts anomalies (Fig. 12b; red shading) reflect cooler near-surface air above warmer seas. These patterns are consistent with suppressed convection and moisture recycling under a stronger IOHP, as discussed in Morioka et al. (2011). Similar results were identified by Alexander and Arblaster (2009), who linked stable stratification to changes in vertical fluxes and reduced convective mixing.

Wind anomalies (Fig. 12c, d) reveal strengthened easterly (negative U) and northward (positive V) flows, reinforcing stability and drying. These circulation patterns are consistent with anticyclonic subsidence and horizontal moisture divergence, which inhibit surface heat fluxes. Results resonate with vector composite findings in Balsamo et al. (2009), where anomalous circulation patterns played a significant role in modulating near-surface atmospheric moisture and heat exchange.

4.6 Composite differences in latent and sensible heat fluxes

The composite analysis of surface fluxes (Fig. 13) further substantiates the suppressive effect of IOHP high phases on energy exchange. LHF anomalies (Fig. 13a) show significant negative values between 15-30º S and 65-95º E, while SHF anomalies (Fig. 13b) concentrate in tropical latitudes. These changes are statistically significant based on 1000-permutation Monte Carlo simulations, indicating robust atmospheric control on flux regulation. The use of Monte Carlo testing to validate flux composite differences is

supported by previous work in the Indo-Pacific sector (Cai et al., 2019; Srinivas et al., 2021).

Overall, the integration of temporal, spatial, and composite analyses confirms the dominant role of IOHP dynamics in regulating heat fluxes across the southeastern Indian Ocean. This modulation is amplified through interactions with IOD, SAM, and ENSO, highlighting the interconnected nature of regional climate variability. The findings resonate with and extend existing literature on the atmospheric control of oceanic surface fluxes (Balsamo et al., 2009; Ummenhofer et al., 2009; Morioka et al., 2011; Romanski and Hameed 2015; Power and Delage 2018; Pepler et al., 2019).

5. Conclusion

This study highlights the critical role of the IOHP system in modulating surface turbulent heat fluxes across the southeastern Indian Ocean during the austral summer (DJF). Using a comprehensive blend of time series analysis, spatial correlations, and Monte Carlo-based composite diagnostics over 1988-2017, we demonstrate that both the intensity and spatial displacement of the IOHP significantly influence latent and sensible heat exchanges between the ocean and atmosphere.

Our results show a pronounced long-term decline in LHF, strongly associated with weakening IOHP pressure and reduced spatial coverage of the high-pressure system. In contrast, SHF remained relatively stationary, exhibiting only interannual fluctuations. These trends support the notion that evaporative cooling has weakened over the region, possibly contributing to observed warming patterns in the Australian climate (Marshall et al., 2006; Timbal and Drosdowsky, 2013).

Furthermore, the longitudinal shift of the IOHP core shows moderate negative correlation with pressure, suggesting eastward displacement during weaker phases. These shifts likely altered the near-surface wind fields and vertical gradients of temperature and humidity, as confirmed by significant composite anomalies in Qa – Qs and Ta – Ts fields. Notably, anomalous northward wind flows and enhanced subsidence under IOHP high conditions may suppress evaporation and cloud formation, consistent with similar findings linking intensified subsidence and reduced cloud cover to upstream convective forcing in the Indo-Pacific sector (Romanski and Hameed 2015; Xia et al., 2024)

Correlation analyses with major climate modes (ENSO, SAM, IOD, SPH) further reinforce these linkages. Negative IOD and La Niña conditions were consistently associated with enhanced latent heat release, especially near western Australia, while positive SAM phases suppressed moisture availability and reinforced high-pressure anomalies (Saji et al., 1999; Pepler et al., 2014; Lim et al., 2016). The SPH system, though centered farther east, still showed a detectable influence in overlapping zones, reinforcing the coupled nature of these subtropical highs (England et al., 2014).

In sum, this work underscores that the decadal weakening and positional shifts of the IOHP system are closely tied to declining oceanic evaporative fluxes and may be a key contributor to regional climate warming. These findings provide a mechanistic basis to understand heatwave intensification in southern Australia (Power et al., 2018) and call for deeper integration of subtropical high dynamics in seasonal forecasting models.

Acknowledgments

The authors acknowledge the Institute of Space Science and Technology (ISST), University of Karachi, for providing the academic environment necessary to complete this research. Nasir Ilyas expresses sincere gratitude to his supervisor, Dr. Jawed Iqbal, for his continuous guidance, and to Faisal Riaz for his helpful input during the analysis. The datasets used in this study were freely accessed from publicly available sources, and the authors appreciate the efforts of the scientific teams in maintaining these repositories. The authors used ChatGPT (GPT-5, OpenAI, 2025) only to assist with formatting of bibliographic references according to the *Atmósfera* journal guidelines.

References

Alam M, Riaz SMF, Iqbal MJ. 2021. The impact of trends in South Asia Low Pressure Center on North Indian Ocean air-sea heat fluxes. Journal of Atmospheric and Solar-Terrestrial Physics 226: 105786. https://doi.org/10.1016/j.jastp.2021.105786

Alexander LV, Arblaster JM. 2009. Assessing trends in observed and modelled climate extremes over Australia in relation to future projections. International Journal of Climatology 29: 417-435. https://doi.org/10.1002/joc.1730

Arblaster JM, Meehl GA, Karoly DJ. 2011. Future climate change in the Southern Hemisphere: Competing effects of ozone and greenhouse gases. Geophysical Research Letters 38: L02701. https://doi.org/10.1029/2010GL045384

Balsamo G, Beljaars A, Scipal K, Viterbo P, van den Hurk B, Hirschi M, Betts AK. 2009. A revised hydrology for the ECMWF model: Verification from field site to terrestrial water storage and impact in the Integrated Forecast System. Journal of Hydrometeorology 10: 623-643. https://doi.org/10.1175/2008JHM1068.1

Cai W, Wu L, Lengaigne M, Li T, McGregor S, Kug J-S, Yu J-Y, Stuecker MF, Santoso A, Li X, Ham Y-G, Chikamoto Y, Ng B, McPhaden MJ, Du Y, Dommenget D, Jia F, Kajtar JB, Keenlyside N, Lin X, Luo J-J, Martín-Rey M, Ruprich-Robert Y, Wang G, Xie S-P, Yang Y, Kang SM, Choi J-Y, Gan B, Kim G-I, Kim C-E, Kim S, Kim J-H, Chang P. 2019. Pantropical climate interactions. Science 363: eaav4236. https://doi.org/10.1126/science.aav4236

Chiu LS, Gao S, Shie C-L. 2013. Satellite-based ocean surface turbulent fluxes. In: Satellite-based applications on climate change (Qu J, Powell A, Sivakumar M, Eds.). Springer, Dordrecht, 165-181. https://doi.org/10.1007/978-94-007-5872-8_11

England MH, McGregor S, Spence P, Meehl GA, Timmermann A, Cai W, Gupta AS, McPhaden MJ, Purich A, Santoso A. 2014. Recent intensification of wind-driven circulation in the Pacific and the ongoing warming hiatus. Nature Climate Change 4: 222-227. https://doi.org/10.1038/nclimate2106

Hendon HH, Thompson DWJ, Wheeler MC. 2007. Australian rainfall and surface temperature variations associated with the Southern Hemisphere Annular Mode. Journal of Climate 20: 2452-2467. https://doi.org/10.1175/JCLI4134.1

Hersbach H, Bell B, Berrisford P, Hirahara S, Horányi A, Muñoz-Sabater J, Nicolas J, Peubey C, Radu R, Schepers D, Simmons A, Soci C, Abdalla S, Abellan X, Balsamo G, Bechtold P, Biavati G, Bidlot J, Bonavita M, De Chiara G, Dahlgren P, Dee D, Diamantakis M, Dragani R, Flemming J, Forbes R, Fuentes M, Geer A, Haimberger L, Healy S, Hogan RJ, Hólm E, Janisková M, Keeley S, Laloyaux P, Lopez P, Lupu C, Radnoti G, de Rosnay P, Rozum I, Vamborg F, Villaume S, Thépaut J-N. 2020. The ERA5 global reanalysis. Quarterly Journal of the Royal Meteorological Society 146: 1999-2049. https://doi.org/10.1002/qj.3803

Holbrook NJ, Scannell HA, Sen Gupta A, Benthuysen JA, Feng M, Oliver ECJ, Alexander LV, Burrows MT, Donat MG, Hobday AJ, Moore PJ, Perkins-Kirkpatrick SE, Smale DA, Straub SC, Wernberg T. 2019. A global assessment of marine heatwaves and their drivers. Nature Communications 10: 2624. https://doi.org/10.1038/s41467-019-10206-z

Kalnay E, Kanamitsu M, Kistler R, Collins W, Deaven D, Gandin L, Iredell M, Saha S, White G, Woollen J, Zhu Y, Chelliah M, Ebisuzaki W, Higgins W, Janowiak J, Mo KC, Ropelewski C, Wang J, Leetmaa A, Reynolds R, Jenne R, Joseph D. 1996. The NCEP/NCAR 40-year reanalysis project. Bulletin of the American Meteorological Society 77: 437-471. https://doi.org/10.1175/1520-0477(1996)077%3C0437:TNYRP%3E2.0.CO;2

Lim EP, Hendon HH, Arblaster JM, Delage F, Nguyen H, Min SK, Wheeler MC. 2016. The impact of the Southern Annular Mode on future changes in Southern Hemisphere rainfall. Geophysical Research Letters 43: 7160-7167. https://doi.org/10.1002/2016GL069453

Mahlobo D, Engelbrecht F, Ndarana T, Abubakar HB, Olabanji MF, Ncongwane K. 2024. Analysis of the Hadley cell subtropical anticyclones and their effect on South African rainfall. Theoretical and Applied Climatology 155: 1035-1054. https://doi.org/10.1007/s00704-023-04674-z

Marshall GJ. 2003. Trends in the Southern Annular Mode from observations and reanalyses. Journal of Climate 16: 4134-4143. https://doi.org/10.1175/1520-0442(2003)016<4134:TITSAM>2.0.CO;2

Marshall GJ, Orr A, van Lipzig NPM, King JC. 2006. The impact of a changing Southern Hemisphere Annular Mode on Antarctic Peninsula summer temperatures. Journal of Climate 19: 5388-5404. https://doi.org/10.1175/JCLI3844.1

MathWorks. 2023. MATLAB R2023a. Available at: https://www.mathworks.com (accessed on April 10, 2025).

Morioka Y, Tozuka T, Yamagata T. 2011. On the growth and decay of the subtropical dipole mode in the South Atlantic. Journal of Climate 24: 5538-5554. https://doi.org/10.1175/2011JCLI4010.1

Morioka Y, Doi T, Behera SK. 2018. Decadal climate predictability in the southern Indian Ocean captured by SINTEX-F using a simple SST-nudging scheme. Scientific Reports 8: 1029. https://doi.org/10.1038/s41598-018-19349-3

Murphy BF, Timbal B. 2008. A review of recent climate variability and climate change in southeastern Australia. International Journal of Climatology 28: 859-879. https://doi.org/10.1002/joc.1627

Pepler A, Timbal B, Rakich C, Coutts-Smith A. 2014. Indian Ocean Dipole overrides ENSO's influence on cool season rainfall across the eastern seaboard of Australia. Journal of Climate 27: 3816-3826. https://doi.org/10.1175/JCLI-D-13-00554.1

Pepler A, Dowdy A, Hope P. 2019. A global climatology of surface anticyclones, their variability, associated drivers and long-term trends. Climate Dynamics 52: 5397-5412. https://doi.org/10.1007/s00382-018-4451-5

Pepler AS, Rudeva I. 2023. Anomalous subtropical zonal winds drive decreases in southern Australian frontal rain. Weather and Climate Dynamics 4: 175-188. https://doi.org/10.5194/wcd-4-175-2023

Perkins-Kirkpatrick SE, White CJ, Alexander LV, Argüeso D, Boschat G, Cowan T, Evans JP, Ekström M, Oliver ECJ, Phatak A, Purich A. 2016. Natural hazards in Australia: Heatwaves. Climatic Change 139: 101-114. https://doi.org/10.1007/s10584-016-1650-0

Power SB, Delage FPD. 2018. El Niño-Southern Oscillation and associated climatic conditions around the world during the latter half of the twenty-first century. Journal of Climate 31: 6189-6207. https://doi.org/10.1175/JCLI-D-18-0138.1

Rehman SU, Khan K, Simmonds I. 2019. Links between Tasmanian precipitation variability and the Indian Ocean subtropical high. Theoretical and Applied Climatology 138: 1255-1267. https://doi.org/10.1007/s00704-019-02891-z

Rehman US, Simmonds I, Usmani BA, Hannachi A. 2024. The role played by the Indian Ocean High in affecting winter precipitation over Victoria, Australia. Dynamics of Atmospheres and Oceans 108: 101484. https://doi.org/10.1016/j.dynatmoce.2024.101484

Romanski J, Hameed S. 2015. The impact of trends in the large-scale atmospheric circulation on Mediterranean surface turbulent heat fluxes. Advances in Meteorology 2015: 519593. https://doi.org/10.1155/2015/519593

Rudeva I, Simmonds I, Crock D, Boschat G. 2019. Midlatitude fronts and variability in the Southern Hemisphere tropical width. Journal of Climate 32: 8243-8260. https://doi.org/10.1175/JCLI-D-18-0782.1

Saji NH, Goswami BN, Vinayachandran PN, Yamagata T. 1999. A dipole mode in the tropical Indian Ocean. Nature 401: 360-363. https://doi.org/10.1038/43854

Simmonds I, Li M. 2021. Trends and variability in polar sea ice, global atmospheric circulations, and baroclinicity. Annals of the New York Academy of Sciences 1504: 167-186. https://doi.org/10.1111/nyas.14673

Srinivas G, Remya PG, Kumar BP, Modi A, Nair TMB. 2021. The impact of Indian Ocean Dipole on tropical Indian Ocean surface wave heights in ERA5 and CMIP5 models. International Journal of Climatology 41: 1619-1632. https://doi.org/10.1002/joc.6900

Stuecker MF, Timmermann A, Jin F-F, McGregor S, Ren H-L. 2013. A combination mode of the annual cycle and the El Niño/Southern Oscillation. Nature Geoscience 6: 540-544. https://doi.org/10.1038/ngeo1826

Sun X, Wu R. 2022. Contribution of wind speed and sea-air humidity difference to the latent heat flux-SST relationship. Ocean-Land-Atmosphere Research 2022: 9815103. https://doi.org/10.34133/2022/9815103

Tandon NF, Gerber EP, Sobel AH, Polvani LM. 2013. Understanding Hadley Cell expansion versus contraction: Insights from simplified models and implications for recent observations. Journal of Climate 26: 4304-4321. https://doi.org/10.1175/JCLI-D-12-00598.1

Taschetto AS, England MH. 2009. El Niño Modoki impacts on Australian rainfall. Journal of Climate 22: 3167-3174. https://doi.org/10.1175/2008JCLI2589.1

Timbal B, Drosdowsky W. 2013. The relationship between the decline of southeastern Australian rainfall and the strengthening of the subtropical ridge. International Journal of Climatology 33: 1021-1034. https://doi.org/10.1002/joc.3492

Ummenhofer CC, England MH, McIntosh PC, Meyers GA, Pook MJ, Risbey JS, Gupta AS, Taschetto AS. 2009. What causes southeast Australia's worst droughts? Geophysical Research Letters 36: L04706. https://doi.org/10.1029/2008GL036801

Van Niel TG. 2023. Latent and sensible heat flux for Australia by scaling flux tower data 2000 to 2023. Version 1. Dataset. Terrestrial Ecosystem Research Network. Available at: https://portal.tern.org.au/metadata/c2ee40f0-4bd1-49a6-8880-31c9054a3675 (accessed on May 18, 2025).

Wilks DS. 2016. "The stippling shows statistically significant grid points": How research results are

routinely overstated and overinterpreted, and what to do about it. Bulletin of the American Meteorological Society 97: 2263-2273. https://doi.org/10.1175/BAMS-D-15-00267.1

Wills RC, Schneider T, Wallace JM, Battisti DS, Hartmann DL. 2018. Disentangling global warming, multidecadal variability, and El Niño in Pacific temperatures. Geophysical Research Letters 45: 2487-2496. https://doi.org/10.1002/2017GL076327

Xia M, Yang S, Wei W, Fan H, Lin S, Deng K. 2024. Intensified western Pacific convection increases the probability of hot extremes in the Middle East during the boreal spring. Journal of Geophysical Research: Atmospheres 129: e2024JD042048. https://doi.org/10.1029/2024JD042048

Yang H, Lohmann G, Shi X, Müller J. 2023. Evaluating the mechanism of tropical expansion using idealized numerical experiments. Ocean-Land-Atmosphere Research 2: 0004. https://doi.org/10.34133/olar.0004

Yu L, Weller RA. 2007. Objectively analyzed air-sea heat fluxes for the global ice-free oceans (1981-2005). Bulletin of the American Meteorological Society 88: 527-539. https://doi.org/10.1175/BAMS-88-4-527